Fe co-doping effect on fluorine-doped tin oxide transparent conducting films accelerating electrochromic switching performance

Myeong-Hun Jo[a,1], Bon-Ryul Koo[b,1], Hyo-Jin Ahn[a,b,*]

[a] Department of Materials Science and Engineering, Seoul National University of Science and Technology, Seoul, 01811, South Korea
[b] Program of Materials Science & Engineering, Convergence Institute of Biomedical Engineering and Biomaterials, Seoul National University of Science and Technology, Seoul, 01811, South Korea

A B S T R A C T

In this study, Fe co-doping into fluorine-doped tin oxide (FTO) films using horizontal ultrasonic spray pyrolysis deposition (HUSPD) is reported as a novel approach to improve their transparent conduction for high-performance electrochromic (EC) devices. To optimize their transparent conducting performance, we adjusted the Fe to F ratio to an atomic percentage of 0, 1, 2, and 3 at% during the film deposition. With the optimized Fe co-doping effect induced at Fe 2 at%, the resulting Fe-doped FTO films exhibited simultaneous improvements in the carrier concentration and Hall mobility which are, attributed to V_o induced by a Fe substitution, and the smooth surface morphology interfering with the growth of the FTO crystallites, respectively. As a result, the Fe-doped FTO films prepared at Fe 2 at% achieve a higher transparent conduction (4.4 ± 0.14 $\Omega/\square$ sheet resistance and 83.1% optical transmittance) than the other films with a figure of merit of $3.56 \times 10^{-2} \, \Omega^{-1}$. Hence, when these unique films are used in EC devices as a transparent conductive oxide, fast switching speeds (6.1 s coloration speed and 5.1 s bleaching speed) and a high coloration efficiency (CE) of 48.2 cm^2/C occur as unique effects of the Fe-doped FTO films, accelerating the insertion of Li^+ and electrons into the WO_3 films, which act as an active EC material and enhancing the electrochemical activity. Therefore, our study provides promising insight into unique transparent conductive oxide films for high-performance EC devices.

1. Introduction

As the problem of energy exhaustion expands into a global social issue, the importance of developing technologies to save energy and increase efficiency has been emphasized. In particular, approximately 60% of the total energy consumed in a building is lost without any effect, which can be solved using smart window technology. Adjusting the solar energy entering a building by using smart windows can reduce the heating and cooling energy consumption by approximately 26% [1,2]. This unique ability is based on electrochromic (EC) devices capable of controlling the optical properties of the materials (e.g. transmittance, reflectivity, and absorbance) via electrical signals. In general, EC devices are composed of two transparent conductive oxide (TCO) films, anodic and cathodic EC materials, and an electrolyte, and are driven by a reversible oxidation/reduction reaction caused by the extraction/insertion of charges in EC materials based on the applied potential [3]. TCO films are an essential component that directly affects EC performance because they transfer electrons formed from an EC material to the external circuit and provide transparency to the devices. Thus, they require ideal properties including a low resistivity ($< 10^{-4} \, \Omega$ cm) and high transmittance ($> 80\%$) [4]. Among various TCO films, such as fluorine-doped tin oxide (FTO), tin-doped indium oxide and aluminum-doped zinc oxide, FTO films are considered a potential TCO film for EC devices owing to their superb transparent conduction and mechanical and chemical stabilities [5]. Given that an acceleration of their transparent conduction is related to performance improvements in EC devices, the fabrication of high-performance FTO films has been attempted using various deposition techniques, such as magnetron sputtering (MS), chemical vapor deposition (CVD), pulsed laser deposition, and ultrasonic spray pyrolysis deposition (USPD) [6]. Although FTO films formed using MS and CVD exhibit superb transparent conduction compared to those prepared by other methods, these techniques have been limited to industrial applications because of their high process cost and restricted processing areas owing to the use of complicated equipment and high vacuum conditions ($< 10^{-4}$ Pa) [7,8]. However, the application of USPD to create a film nanostructure

---

using the formation of precursor droplets (1–100 μm in size) through the ultrasonic atomization is an interesting deposition approach with a notable ability to uniformly coat a large area at a low cost [9]. In addition, this may adjust the characterization of FTO films by adjusting the process parameters (e.g. the deposition temperature and deposition time) and the conditions of the precursor solution (e.g. the functional group and additives) [10,11]. For example, Agashe et al. reported that as the deposition time of FTO films increases when using USPD, their sheet resistance (R_{sh}) gradually decreases due to the increase in carrier concentration, whereas their optical transmittance degrades [10]. Luangchaisri et al. also showed that increasing the $NH_4F/SnCl_4$ ratio to 10 mol% in FTO films causes a decrease in R_{sh}, owing to the increased number of electrons induced by the substitution of F for O atoms [11]. However, with a greater amounts of F, oxygen vacancies (V_o) become filled, or the formation of excessive ionized F atoms act as scattering centers on the FTO, increasing the R_{sh} of the FTO films. At this point, it should be noted that balancing the F substitution with the effect of V_o as a carrier in FTO films is a sensational approach to improving their transparent conduction for use in high-performance EC devices, but has yet to be reported.

In this study, we newly developed Fe-doped FTO films as TCOs for high-performance EC devices using horizontal ultrasonic spray pyrolysis deposition (HUSPD, Ceon, Nano SPD, TV500, Korea). The Fe co-doping effect in FTO films produces an effective supply of charge carriers by introducing V_o into FTO to improve their transparent conduction. Therefore, the Fe atomic percentage into F during the film deposition was adjusted in an effort to optimize their transparent conduction and demonstrate a mechanism to improve the performance of EC devices using Fe-doped FTO films.

2. Experimental details

2.1. Experimental

FTO films with different Fe co-doping were fabricated using HUSPD (Ceon, Nano SPD, TV500, Korea) on a glass substrate (Corning EAGLE XG^{TM}). First, the precursor solution for film deposition was obtained by dissolving 0.68 M tin chloride pentahydrate ($SnCl_4 \cdot 5H_2O$, SAMCHUN) and 1.20 M ammonium fluoride (NH_4F, Aldrich) into de-ionized (DI) water with 5 vol% ethyl alcohol (C_2H_5OH, Duksan). After stirring, iron (III) nitrate nonahydrate chloride ($Fe(NO_3)_3 \cdot 9H_2O$) was added to the transparent FTO solution. The atomic percentage of Fe to F ratio was then controlled at 0, 1, 2, and 3 at% to optimize the transparent conduction of the resulting films. HUSPD was then applied by allowing the droplet formed from the precursor solution using an ultrasonic atomizer (1.6 MHz) to reach a substrate temperature of 420 °C during a 28 min period. The other conditions of the HUSPD were fixed uniformly to a 15 L/min flow rate of the air carrier gas and 5 rpm rotational speed of the substrate, thus yielding four types of FTO films using Fe atomic percentages of 0, 1, 2, and 3 at% (hereafter referred to as bare FTO, 1Fe-FTO, 2Fe-FTO, and 3Fe-FTO, respectively). To characterize the EC performance using the Fe-doped FTO films as the TCO, we utilized WO_3 films as the active EC material. To prepare the WO_3 films, 10 wt% tungsten (VI) chloride (WCl_6, Aldrich) was dissolved into 2-propanol ((CH_3)$_2$CHOH, Aldrich), and the obtained sol solution was then spin-coated for 30 s at 2000 rpm on all Fe-doped FTO films. This was repeated twice. Thereafter, by annealing the samples at 300 °C in air, four types of EC electrodes consisting of WO_3 films and Fe-doped FTO films (bare FTO, 1Fe-FTO, 2Fe-FTO, and 3Fe-FTO) were obtained.

2.2. Characterization

The crystal structure and chemical bonding of the films were analyzed using X-ray diffraction (XRD, Rigaku D/Max − 2500 diffractometer using Cu K_α radiation) and X-ray photoelectron spectroscopy (XPS, ESCALAB 250 equipped with an Al K_α X-ray source), respectively. The morphological and topographical properties of the films were characterized using field-emission scanning electron microscopy (FESEM, Hitachi S − 4800) and atomic force microscopy (AFM, diDimension^{TM} 3100). The electrical and optical properties were characterized using a Hall-effect measurement system (Ecopia, HMS-3000) and ultraviolet–visible (UV–vis) spectroscopy (Perkim − Elmer, Lambda − 35), respectively. The electrochemical properties and EC performances were measured in a three-electrode system, consisting of a reference electrode with Ag wire and a counter electrode with Pt wire, and 1 M of a LiClO$_4$ electrolyte on a potentiostat/galvanostat (PGSTAT302 N, FRA32 M, Metrohm Autolab B.V., Netherlands) at a scan rate of 20 mV/s from − 0.7 to 1.0 V. The in situ optical transmittances at a wavelength of 633 nm during the coloration and bleaching processes were traced using ultraviolet–visible (UV–vis) spectroscopy (Perkim − Elmer, Lambda − 35). The electrochemical impedance spectroscopy (EIS) measurement was carried out on a potentiostat/galvanostat (PGST302 N, Eco Chemie) by applying a sinusoidal signal of 10 mV amplitude within a frequency range from 0.1 Hz to 100 kHz.

3. Results and discussion

Fig. 1a shows the XRD curves obtained from bare FTO, 1Fe-FTO, 2Fe-FTO, and 3Fe-FTO. Bare FTO emits characteristic diffraction peaks at the (110), (101), (200), and (211) planes, which indicates ~26.61°, ~33.87°, ~37.86°, and ~51.75° tetragonal rutile SnO$_2$ (space group P42/mnm [136], JCPDS no. 88–0287), respectively. These diffraction peaks are in a slightly lower position than those of pure SnO$_2$ ((110) plane at ~26.65°, (101) plane at ~33.90°, (200) plane at ~37.98°, and (211) plane at ~51.82°), which indicates a successful formation of the FTO phases through the substitution with larger F$^-$ (ionic radius of 0.133 nm) than the smaller O^{2-} (0.132 nm) of SnO$_2$, as explained by Bragg's equation ($n\lambda = 2d\sin\theta$) [6]. In Fig. 1b, it should be that the
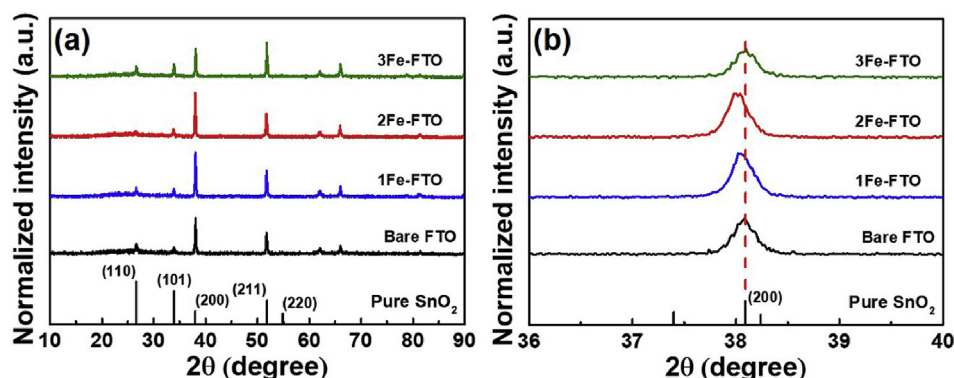

Fig. 1. XRD curves and magnified curves in the range from 36 to 40° of bare FTO, 1Fe-FTO, 2Fe-FTO, and 3Fe-FTO.
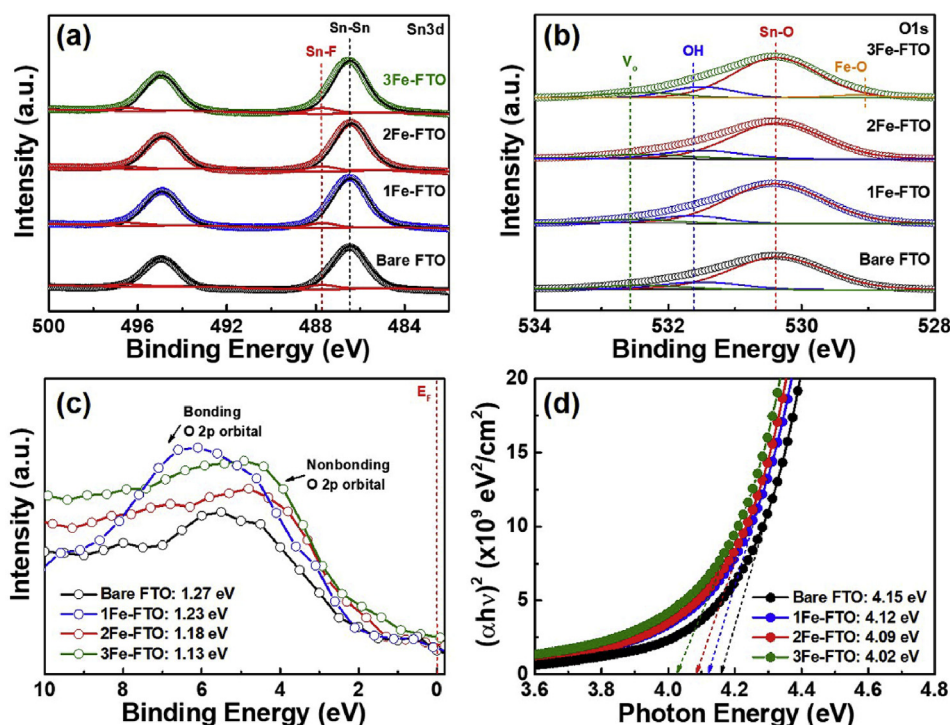
Fig. 2. XPS spectra of (a) Sn 3d and (b) O 1s obtained from all films, (c) valence band spectra, and optical bandgap obtained by relationship between the absorption coefficient (α) and the incident photon energy (hν).

peak shift of the (200) plane toward a low angle is accelerated from bare FTO to 2Fe-FTO, which can result from the substitution of Fe^{3+}, which has higher ionic radius (0.078 nm) than Sn^{4+} (0.069 nm) for FTO [12]. This result can lead to an enhanced carrier concentration as the result of the formation of V_o on the FTO films [13]. In addition, the increase in the (200)/(110) peak ratio from 6.5 for bare FTO to 16.5 for 2Fe-FTO should be noted, and corresponds to the preferred growth of the (200) orientation parallel to the substrate as a result of growth relaxation of the {101} twin planes positioned at the corner of the SnO_2 crystallites due to NO_2 gas generated by the pyrolysis of $Fe(NO_3)_3 \cdot 9H_2O$ [14–16]. However, for 3Fe-FTO, there is relaxation of the (200) peak shift and (200)/(110) peak ratio (4.0) compared to 2Fe-FTO, which may be due to an excessive amount of Fe, causing decrease in the transparent conduction of the FTO films.

To derive the chemical binding states of all films, XPS analysis was conducted as shown in Fig. 2a. All binding energies were realigned by C 1s (284.5 eV) as a reference. In Fig. 2a, for all films, the characteristic peaks of XPS Sn $3d_{5/2}$ and Sn $3d_{3/2}$ are emitted equally at ~486.4 and ~494.9 eV, respectively, indicating a Sn–Sn bond related to Sn^{4+} of the SnO_2 phase [17]. In addition, emission of the binding energy occurs at ~487.7 eV for XPS Sn $3d_{5/2}$ and ~496.4 eV for Sn $3d_{3/2}$, which indicates that the Sn–F is an effect of F-substitution in the SnO_2 phases [17,18]. Interestingly, the XPS Sn 3d spectra of all films show a decreased area ratio of Sn–F to Sn–Sn with increasing the Fe atomic percentage, indicating a gradual decrease in the F-doping concentration on the FTO films (2.69 at% for bare FTO, 2.59 at% for 1Fe-FTO, 2.55 at % for 2Fe-FTO, and 2.48 at% for 3Fe-FTO). Moreover, it is shown in the XPS O 1s spectra of Fig. 2b that the area ratio of V_o (~532.4 eV) to Sn–O (~530.3 eV) increases from bare FTO to 2Fe-FTO, and then decreases when the Fe atomic percentage is 3 at% (3Fe-FTO), which indicates that 2Fe-FTO (5.9 at%) has a higher V_o than the other films (4.4 at% for bare FTO, 5.4 at% for 1Fe-FTO, and 5.3 at% for 3Fe-FTO) owing to the optimized effect of Fe co-doping into the FTO films. This result can be associated with the increasing carrier concentration on the FTO films from the improvement in V_o, which provides two electrons though the F-doping concentration when only one electron is decreased [4,6].

Because V_o of FTO is introduced near valence band edge position, the formation of V_o on the FTO films due to the Fe co-doping effect is also confirmed by the peak position moving toward the Fermi level (EF, binding energy = 0 eV) of the valence band maximum (VBM), determined by linear extrapolation of a nonbonding O 2p orbital on the valence-band XPS spectra, as shown in Fig. 2c [19,20]. That is, as part of the Fe-co doping effect, the Fe^{3+} substituting Sn^{4+} in the SnO_2 lattices can cause a lifting of the valence band by the improved V_o, thus generating a bandgap that narrows from bare FTO to 2Fe-FTO (see Fig. 2d) [13,21]. For 3Fe-FTO, there is a decrease in V_o (5.3 at%) despite the larger amount of Fe, which may be due to the existence of the Fe–O phase, as confirmed through the O 1s XPS spectra, thus affecting the relaxation of the carrier concentration in the FTO films.

Fig. 3 shows the top-view FESEM images of (a) bare FTO, (b) 1Fe-FTO, (c) 2Fe-FTO, and (d) 3Fe-FTO prepared by a different Fe atomic percentage. The surface morphology of all films is interlocked with polyhedral crystallites throughout the surface. Interestingly, as the atomic percentage of Fe increases to 3 at%, their polyhedral crystallite sizes (~222.0–309.6 nm (approximately 257.9 nm) for bare FTO, ~180.5–254.5 nm (approximately 213.2 nm) for 1Fe-FTO, ~151.5–225.3 nm (approximately 187.7 nm) for 2Fe-FTO, and ~135.3–221.7 nm (approximately 173.0 nm) for 3Fe-FTO) gradually decreased, which can be the induced by the existence of the Fe element in the FTO films interfering with the growth of the FTO crystallites, causing a smooth surface morphology to relax the surface scattering for improving the Hall mobility of the transparent conducting oxide films [13,22]. This is also confirmed by the AFM results showing a decrease in the highest root mean square roughness (R_{ms}) from ~30.0 nm for bare FTO to ~24.0 nm for 2Fe-FTO. However, despite the decreased polyhedron-shaped crystallite size of 3Fe-FTO, a higher R_{ms} value is observed than that of 2Fe-FTO, which may be due to the growth of the rod-shaped crystallites via a reorientation effect caused by excessive Fe, thus resulting in a rough surface morphology that can decrease the Hall mobility of the transparent conducting films [23]. Therefore, the XRD, XPS, and SEM results are expected to show that the Fe-doped FTO film formed particularly at 2 at% Fe (2Fe-FTO) is optimized to improve the
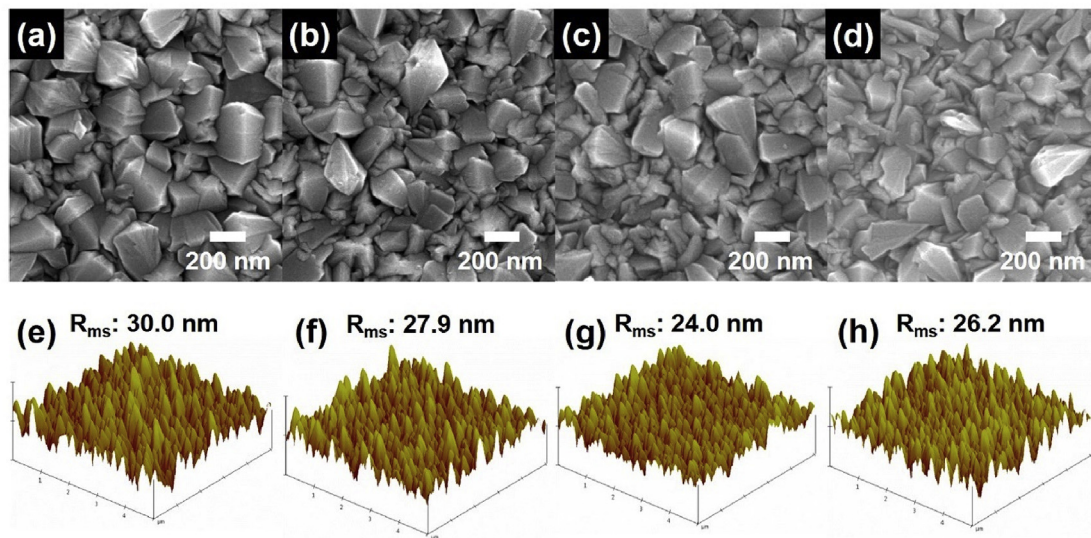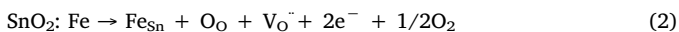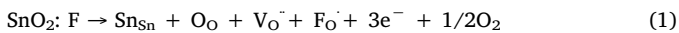
Fig. 3. (a–d) Top-view FESEM and (e–h) AFM images of bare FTO, 1Fe-FTO, 2Fe-FTO, and 3Fe-FTO, respectively.

carrier concentration (*N*) and Hall mobility (*μ*) by a higher V_o and smoother surface morphology of the TCO films for achieving a high EC performance.

Fig. 5a shows the dependence of Fe co-doping on the electrical properties of the FTO films. In general, the resistivity of the TCO films is mainly dependent on their *N* and *μ* values [24]. When the Fe atomic concentration increases from 0 at% (bare FTO) to 2 at% (2Fe-FTO), *N* is enhanced from 6.26×10^{20} to 7.31×10^{20} cm^{-3} due to the increased V_o by the effect of the Fe-co doping into the FTO films, which is induced by the following equations:
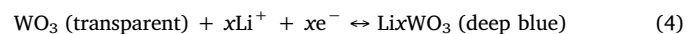
$$SnO_2: F \rightarrow Sn_{Sn} + O_O + V_O^{..} + F_O^. + 3e^- + 1/2O_2 \quad (1)$$

$$SnO_2: Fe \rightarrow Fe_{Sn} + O_O + V_O^{..} + 2e^- + 1/2O_2 \quad (2)$$

The improvement in *μ* is also revealed to range from 24.06 cm^2/(V s) for bare FTO to 34.92 cm^2/(V s) for 2Fe-FTO, which results from the formation of a smooth surface morphology with (200) preferred orientations. However, any further increase in the Fe atomic concentration (3Fe-FTO) can decrease both *N* and *μ*, owing to relaxation of V_o and the (200) preferred orientations, respectively, as a result of the Fe–O phases formed. Based on these variations, we calculate the resistivity (ρ) of the FTO films using the following equation [25]:

$$\rho = 1/(N\mu e) \quad (3)$$

where *N* is the carrier concentration (cm^{-3}), *μ* is the hall mobility (cm^2/(V s)), and *e* is the electron charge (1.60×10^{-19} C). As shown in Table 1, 2Fe-FTO possesses higher electrical performance than the other films. Its superb performance is attributed primarily to the improvement of both *N* and *μ* induced by the optimized Fe co-doping effect; the increased *N* results from the increase in V_o, and the improved *μ* originates from the smooth surface morphology with a (200) preferred orientation. Fig. 4b shows the wavelength dependence on the optical transmittances of the FTO films with the Fe co-doping effect. It can be

seen that the average optical transmittance (*T*) within the range of 400–700 nm gradually decreases from 85.1% for bare FTO to 82.5% for 3Fe-FTO. This variation in the average *T* can be determined by the narrowed bandgap of the FTO films. Therefore, the figure of merit ($\varphi = T^{10}/R_{sh}$) calculated from *T* and the sheet resistance (R_{sh}) of the films used to predict the comprehensive efficiency as a TCO film is the highest for 2Fe-FTO compared to the other films, which is mainly due to the decreased R_{sh} induced by improvements in *N* and *μ*, indicating the implementation of superb transparent conduction in the a TCO film for EC devices [26].

Fig. 5a shows the CV curves of the electrodes using WO_3 to investigate the electrochemical behavior of bare FTO, 1Fe-FTO, 2Fe-FTO, and 3Fe-FTO as TCO films for EC devices. The CV curves of all electrodes emit a pair of redox peaks related to a reduction in a negative potential of the WO_3 and oxidation at positive potential, thus demonstrating the EC behavior from deep blue in a colored state to transparent in a bleached state due to the intercalation and deintercalation of Li$^+$ and electrons, which can be represented by the following equation [27]:

$$WO_3 \text{ (transparent)} + x\text{Li}^+ + xe^- \leftrightarrow \text{Li}x\text{WO}_3 \text{ (deep blue)} \quad (4)$$

It should be noted that 2Fe-FTO has a higher CV area with increasing current densities of both the anodic and cathodic peaks compared to the other films, which indicates an enhancement in the electrochemical activity for a high EC performance by decreased R_{sh} of the Fe-doped FTO films. This offers an effective transport of a large quantity of Li$^+$ and electrons in the WO_3 films [28]. The EC performance with the Fe co-doping effect on the FTO films used as TCO films was characterized by comparing the *in situ* optical transmittance curves of all electrodes, traced through a collaboration of a double-step chronoamperometry (CA) method under an applied potential of −0.7 V (colored state) and 1.0 V (bleached state) for 60 s, and the resultant *in-*

Table 1
List of electrical and optical properties obtained from all Fe-doped FTO films.

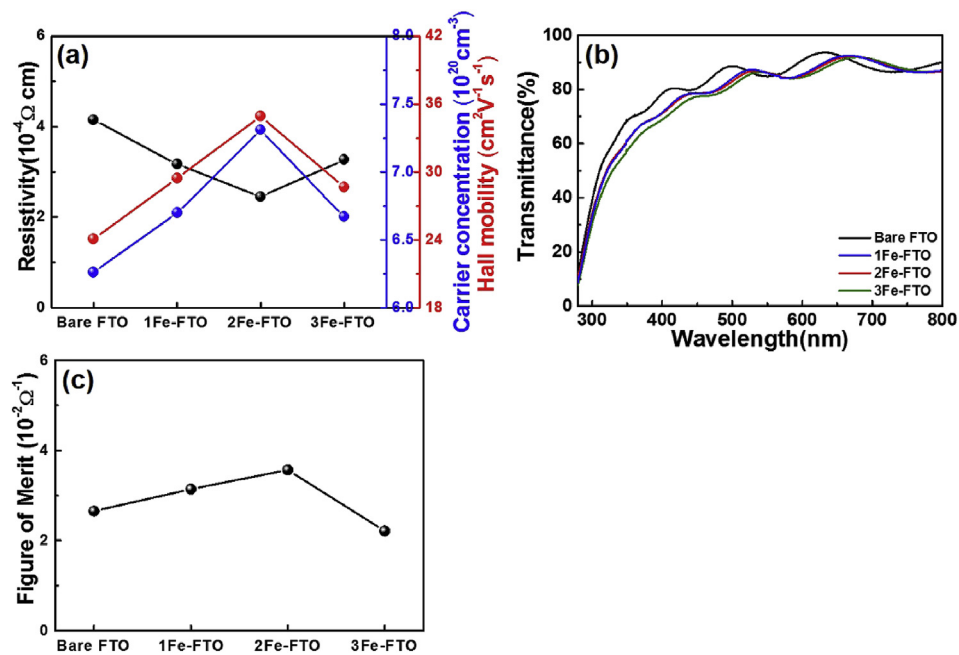|	Bare FTO	1Fe-FTO	2Fe-FTO	3Fe-FTO
Carrier concentration (cm^{-3})	6.26×10^{20}	6.70×10^{20}	7.31×10^{20}	6.67×10^{20}
Hall mobility (cm^2/(V s))	24.06	29.44	34.92	28.66
Resistivity (Ω cm)	4.15×10^{-4}	3.17×10^{-4}	2.45×10^{-4}	3.27×10^{-4}
Sheet resistance (Ω/□)	7.5 ± 0.24	5.7 ± 0.19	4.4 ± 0.14	6.6 ± 0.23
Transmittance (%)	85.1	84.2	83.1	82.5
Figure of Merit ($\times 10^{-2} \Omega^{-1}$)	2.65	3.14	3.56	2.21

Fig. 4. Curves showing (a) electrical properties with carrier concentration, Hall mobility, and resistivity, (b) optical transmittance traced in wavelength range of 300–800 nm, and FOM value of all films.

situ transmittance variation at λ_{633nm}. As shown in Fig. 5b and Table 2, this curve provides two main EC performances: the transmittance modulation ($\triangle T = T_b – T_c$, where T_b is the transmittance in a bleached state and T_c is the transmittance in a colored state) and the switching speed (the time it takes to reach 90% of the full transmittance modulation) [29]. For $\triangle T$, there is a minute improvement from 52.7% for bare FTO to 53.7% for 2Fe-FTO owing to the increased electrochemical activity decreasing the transmittance value in a colored state, which is caused by the increased electrochemical activity. In contrast, the optical bandgap, which gradually narrows as the Fe atomic concentration is

improved to 3 at%, decreases the transmittance value in bleached state, thus causing a decrease in $\triangle T$ of 3Fe-FTO as an extra effect of the degraded electrochemical activity. For the switching speed, it should be noted that 2Fe-FTO has higher values (6.1 s for the coloration speed and 5.1 s for the bleaching speed) than those using the other films, which is attributed primarily to the acceleration of Li^+ and electron diffusion on the WO_3 films due to the decrease in R_{sh}. In addition, the CE is another important EC performance defined as the optical density (OD) with the intercalated charge densities (Q/A) (see Eq. (3)–(4)) [28,29].
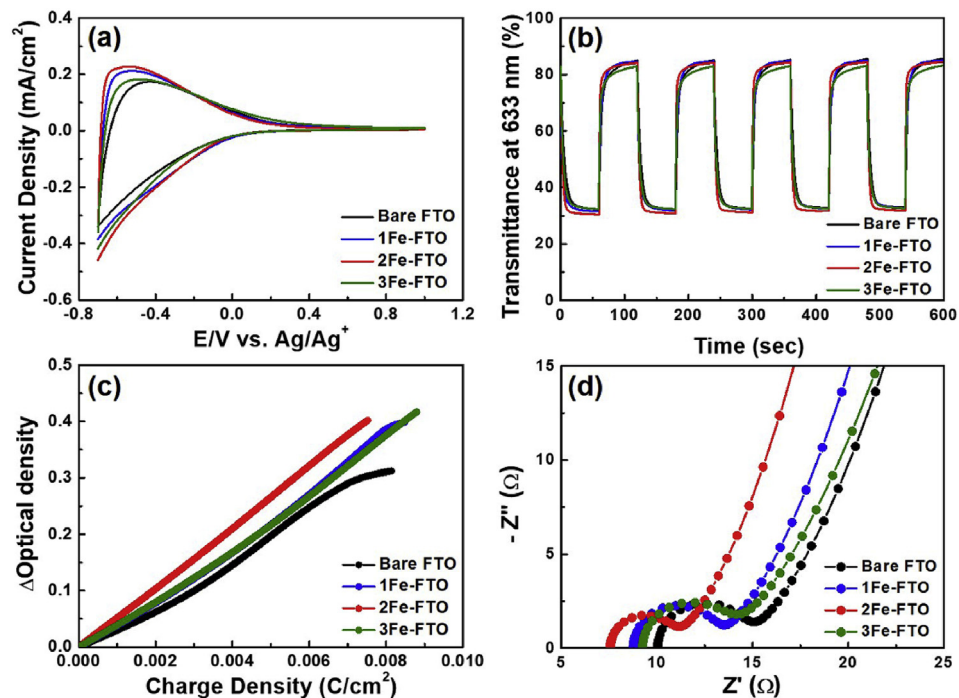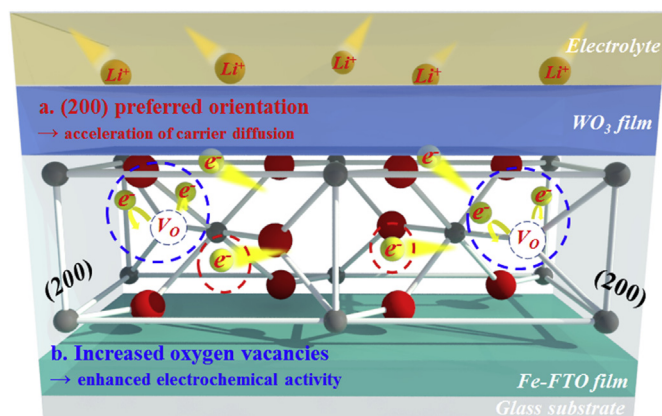
$$CE = \triangle OD/(Q/A) \qquad (5)$$

Fig. 5. (a) CV curves recorded in potential of -0.7-1.0 V at the scan rate of 20 mV/s, (b) *In situ* optical transmittances spectra at different applied potential for 60 s (-0.7 V for colored state and 1.0 V for bleached state), and (c) OD curve at 633 nm and (d) Nyquist plot as a function of intercalated charge density of -0.7 V.

Table 2
Comparison of EC performances with other previous works using FTO films as TCO and WO_3 as EC active material.

Samples	Transmittance modulation (%, 633 nm)	Coloration speed (s)	Bleaching speed (s)	CE (cm²/C)
WO_3-FTO 1 [26]	52.5	12.1	13.9	37.2
WO_3-FTO 2 [31]	52.1	12.1	12.5	38.5
WO_3-FTO 3 [32]	44.4	6.4	7.0	47.8
WO_3-FTO 4 [33]	61.0	–	–	39.4
WO_3–2Fe-FTO (Our result)	53.7	6.1	5.1	48.2

Fig. 6. Schematic illustration of improving EC performances on Fe-doped FTO films.

$$\triangle OD = \log(T_b/T_c) \tag{6}$$

where Q is the charge capacity and A is the given electrode area. As shown in Fig. 5c, the CE values obtained by sloping the OD curve of 633 nm with the intercalated charge density at -0.7 V indicate that the CE of 2Fe-FTO is higher than that of the other films, which may arise the broadened $\triangle T$ with effective transport of Li^+ and electron in the WO_3 film. This phenomenon is confirmed by the EIS result shown in Fig. 5d. To use 2Fe-FTO as a TCO of an EC device, it should be noted that the charge-transfer resistance (R_{ct}) is lower than that using the other electrodes, which can be induced by the lower series resistance (R_s) resulting from of their decreased R_{sh} [6,30]. Therefore, the results indicate that Fe-doped FTO formed at Fe atomic percentage of 2 at% can realize the optimum and competitive EC performances with other previous works (Table 2), including fast switching speeds (6.1 s for the coloration speed and 5.1 s for the bleaching speed) [26,31–33]. As shown in Fig. 6, this is caused by the improved transport of Li^+ and electrons on the WO_3 films by the smooth surface morphology with a (200) preferred orientation, which decreases surface scattering and achieves a good CE (48.2 cm²/C) owing to the high electrochemical activity. $\triangle T$ is thereby broadened with an effective behavior of Li^+ and electrons in the WO_3 films as an effect of the increased V_o forming more carriers.

4. Conclusion

Fe-doped FTO films were fabricated by optimizing the Fe atomic concentration used as a co-doping source. The effect of the increased Fe atomic concentration to 2 at% caused an increase in V_o, thereby providing more electrons compared to the result from F doping and formation of smooth surface morphology with (200) preferred orientations to relax the surface scattering. This suggest that both carrier concentration and Hall mobility should be increased, thus resulting in a decreased in R_{sh} of the Fe-doped FTO films. As a result, the EC electrodes with optimized Fe-doped FTO films (2Fe-FTO) used as a TCO film show good performance for an EC device with fast switching speeds (6.1 s for the coloration speed and 5.1 s for the bleaching speed)

and a high CE (48.2 cm²/C), which is a higher than that of using other films. Fast switching speeds are induced from the faster transport of Li^+ and electrons in the WO_3 films by a smooth surface morphology with a (200) preferred orientation, and a high CE value is results from broadening $\triangle T$ by an enhancement of the electrochemical activity as the result of the increased V_o. Therefore, we believe that unique Fe-doped FTO films can be used as valuable TCO films for high-performance EC devices.

Declaration of competing interest

The authors declare that they have no known competing financial interests or personal relationships that could have appeared to influence the work reported in this paper.

Acknowledgements

References

[1] A. Paolela, C. Faure, V. Timoshevskii, S. Mrras, G. Bertoi, A. Guerfi, A. Vijh, M. Armand, K. Zaghib, A review on energy storage hexacyanoferrate-based materials for and smart windows: challenges and perspectives, J. Mater. Chem. 5 (2017) 18919–18932.

[2] M. Rakibuddin, H. Kim, Synthesis and characterization of facile industrially scalable and cost effective WO_3 micro–nanostructures for electrochromic devices and photocatalyst, Ceram. Int. 44 (2018) 16615–16623.

[3] Q. Zhao, Y. Fang, K. Qiao, W. Wei, Y. Yao, Y. Gao, Printing of WO_3/ITO nanocomposite electrochromic smart windows, Sol. Energy Mater. Sol. Cells 194 (2019) 95–102.

[4] B.-R. Koo, J.-W. Bae, H.-J. Ahn, Optoelectronic multifunctionality of combustion-activated fluorine-doped tin oxide films with high optical transparency, Ceram. Int. 45 (2019) 10260–10268.

[5] B. Zhang, Y. Tian, J.X. Zhang, W. Cai, The role of oxygen vacancy in fluorine-doped SnO_2 films, Phys. B 406 (2011) 1822–1826.

[6] B.-R. Koo, D.-H. Oh, D.-H. Riu, H.-J. Ahn, Improvement of transparent conducting performance on oxygen activated fluorine-doped tin oxide electrodes formed by horizontal ultrasonic spray pyrolysis deposition, ACS Appl. Mater. Interfaces 9 (2017) 44584–44592.

[7] T. Maruyama, H. Akagi, Fluorine-doped tin dioxide thin films prepared by radio-frequency magnetron sputtering, J. Electrochem. Soc. 143 (1996) 283–287.

[8] N. Noor, I.P. Parkin, Enhanced transparent-conducting fluorine-doped tin oxide films formed by aerosol-assisted chemical vapour deposition, J. Mater. Chem. C 1 (2013) 984–996.

[9] D.-Y. Shin, B.-R. Koo, H.-J. Ahn, Lithium storage kinetics of highly conductive F-doped SnO_2 interfacial layer on lithium manganese oxide surface, Appl. Surf. Sci. 499 (2020) 144057.

[10] C. Agashe, J. Hüpkes, G. Schöpe, M. Berginski, Physical properties of highly oriented spray-deposited fluorine-doped tin dioxide films as transparent conductor, Sol. Energy Mater. Sol. Cells 93 (2009) 1256–1262.

[11] C. Luangchaisri, S. Dumrongrattana, P. Rakkwamsuk, Effect of heat treatment on electrical properties of fluorine doped tin dioxide films prepared by ultrasonic spray pyrolysis technique, Procedia Eng. 32 (2012) 663–669.

[12] D.V. Wellia, Q.C. Xu, M.A. Sk, K.H. Lim, T.M. Lim, T.T.Y. Tan, Experimental and theoretical studies of Fe-doped TiO_2 films prepared by peroxo sol–gel method, Appl. Catal. Gen. 401 (2011) 98–105.

[13] J.-W. Bae, B.-R. Koo, H.-J. Ahn, Fe doping effect of vanadium oxide films for enhanced switching electrochromic performances, Ceram. Int. 45 (2019) 7137–7342.

[14] K. Murakami, I. Yagi, S. Kaneko, Oriented growth of tin oxide thin films on glass substrates by spray pyrolysis of organotin compounds, J. Am. Ceram. Soc. 79 (1996)

2557–2562.

[15] A. Franco Jr., T.E.P. Alves, E.C.O. Lima, E.S. Nunes, V. Zapf, Enhanced magneti-zation of nanoparticles of $Mg_xFe_{(3-x)}O_4$ ($0.5 \leq x \leq 1.5$) synthesized by combustion reaction, Appl. Phys. Lett. A Mater. Sci. Process 94 (2009) 131–137.

[16] D. Miao, Q. Zhao, S. Wu, Z. Wang, X. Zhang, X. Zho, Effect of substrate temperature on the crystal growth orientation of SnO_2:F thin films spray-deposited on glass substrates, J. Non Cryst. Sol. 356 (2010) 2557–2561.

[17] B.-R. Koo, H.-J. Ahn, Structural, electrical, and optical transparent conductive oxides properties of Sb-doped SnO_2 fabricated using an electrospray technique, Ceram. Int. 40 (2014) 4375–4381.

[18] H.-G. Jung, C.S. Yoon, J. Prakash, Y.-K. Sun, Mesoporous anatase TiO_2 with high surface area and controllable pore size by F^--ion doping: applications for high-power li-ion battery anode, J. Phys. Chem. C 113 (2009) 21258–21263.

[19] B.-R. Koo, D.-H. Oh, H.-J. Ahn, Influence of Nb-doped TiO_2 blocking layers as a cascading band structure for enhanced photovoltaic properties, Appl. Surf. Sci. 433 (2018) 27–34.

[20] P. Li, H. Wang, J. Xu, H. Jing, H. Han, F. Lu, Reduction of CO_2 to low carbon alcohols on CuO FCs/Fe_2O_3 NTs catalyst with photoelectric dual catalytic inter-faces, Nanoscale 5 (2013) 11748–11754.

[21] T.N. Soitah, C. Yang, L. Sun, Structural, optical and electrical properties of Fe-doped SnO_2 fabricated by sol–gel dip coating technique, Mater. Sci. Semicond. Process. 13 (2010) 125–131.

[22] Z. Wang, Q. Tang, B. He, X. Chen, H. Chen, L. Yu, Titanium dioxide/calcium fluoride nanocrystallite for efficient dye-sensitized solar cell. A strategy of enhan-cing light harvest, J. Power Sources 275 (2015) 175–180.

[23] A.A. Yadav, S.C. Pawar, D.H. Patil, M.D. Ghogare, Properties of (200) oriented, highly conductive SnO_2 thin films by chemical spray pyrolysis from non-aqueous medium: effect of antimony doping, J. Alloy. Comp. 652 (2015) 145–152.

[24] B. Sarma, D. Barman, B.K. Sarma, AZO (Al:ZnO) thin films with high figure of merit as stable indium free transparent conducting oxide, Appl. Surf. Sci. 479 (2019) 786–795.

[25] B.-R. Koo, J.-W. Bae, H.-J. Ahn, Low-temperature conducting performance of transparent indium tin oxide/antimony tin oxide electrodes, Ceram. Int. 43 (2017) 6124–6129.

[26] K.-H. Kim, B.-R. Koo, H.-J. Ahn, Sheet resistance dependence of fluorine-doped tin oxide films for high performance electrochromic devices, Ceram. Int. 44 (2018) 9408–9413.

[27] C. Hua, G. Yuan, Z. Cheng, H. Jiang, G. Xu, Y. Liu, G. Han, Building architecture of TiO_2 nanocrystals embedded in amorphous WO_3 films with improved electro-chromic properties, Electrochim. Acta 309 (2019) 354–361.

[28] M. Wang, Q. Liu, G. Dong, Y. He, X. Diao, Influence of thickness on the structure, electrical, optical and electrochromic properties of AZO thin films and their in-organic all-solid-state devices, Electrochim. Acta 258 (2017) 1336–1347.

[29] B.-R. Koo, J.-W. Bae, H.-J. Ahn, Percolation effect of V_2O_5 nanorod/graphene oxide nanocomposite films for stable fast-switching electrochromic performances, Ceram. Int. 45 (2019) 12325–12330.

[30] L. Qiu, H. Zhang, W. Wang, Y. Chen, R. Wang, Effects of hydrazine hydrate treat-ment on the performance of reduced graphene oxide film as counter electrode in dye-sensitized solar cells, Appl. Surf. Sci. 319 (2014) 339–343.

[31] K.-H. Kim, B.-R. Koo, H.-J. Ahn, Effects of Sb-doped SnO_2-WO_3 nanocomposite on electrochromic performance, Ceram. Int. 45 (2019) 15990–15995.

[32] D. Zhou, F. Shi, D. Xie, D.H. Wang, X.H. Xia, X.L. Wang, C.D. Gu, J.P. Tu, Bi-functional Mo-doped WO_3 nanowire array electrochromism-plus electrochemical energy storage, J. Colloid Interface Sci. 465 (2016) 112–120.

[33] A.A. Joraid, Comparison of electrochromic amorphous and crystalline electron beam deposited WO_3 thin films, Curr. Appl. Phys. 9 (2009) 73–79.